




Large eddy simulation of power-law fluid dam break wave impacting against a vertical wall

Andrea Del Gaudio ¹, George Constantinescu ², Cristiana Di Cristo,¹
Francesco De Paola ¹ and Andrea Vacca¹

¹*Department of Civil and Environmental Engineering, IIHR Hydraulics and Engineering, University of Iowa, Iowa City, Iowa 52242, USA*

²*Dipartimento di Ingegneria Civile, Edile e Ambientale, Università di Napoli “Federico II”, Via Claudio 21, 80125 Napoli, Italy*



(Received 6 February 2024; accepted 29 May 2024; published 8 July 2024)

The study investigates the evolution of a dam break wave of a mixture of clay and water in turbulent flow conditions and its interaction with a vertical rigid wall. The phenomenon reproduction, important for planning risk mitigation strategies and designing protective structures, is performed by means of three-dimensional large eddy simulations. The dynamical Smagorinsky model is employed and the volume-of-fluid technique is used to calculate the free surface evolution with time. A power-law model is considered to represent the mixture rheology. With reference to a small-scale setup, the paper analyzes the influence of the clay concentration and of initial fluid depth upstream of the lock gate on the temporal evolution of the front, the bed shear stresses, and the force acting on the vertical endwall. Moreover, the presence of three-dimensional effects and the turbulence role are also investigated. The occurrence of scale effects for the non-Newtonian dam break wave is finally examined by performing an additional test with a larger-scale setup. Results indicate that lobelike structures develop near the front of the current and near-bed streaks of low and high velocity are present behind the front. The variation of the wave front position with time is described by a power-law function, independently of both clay concentration and initial fluid depth. Over the body of the current, the nondimensional bed shear stress values in the simulations performed with non-Newtonian fluids are about two times larger than the ones in the clear water case. Moreover, the peak value of the nondimensional impact force, slightly lower than the one in clear water, decreases when clay concentration is increased. Comparing large- and small-scale tests, higher nondimensional propagation speeds and bed shear stress values in the front region are observed in the former one. Conversely, the nondimensional peak force is not affected by scale effects, suggesting that small-scale tests can be used to provide reliable predictions of this critical variable for engineering design.

DOI: [10.1103/PhysRevFluids.9.074801](https://doi.org/10.1103/PhysRevFluids.9.074801)

I. INTRODUCTION

Mudflows, snow avalanches, debris flows, and submarine landslides are widespread natural hazards to humans and infrastructure (e.g., disrupted roadways and railways and broken electrical, water, and gas lines). To limit damages and loss of life, adequate countermeasures must be implemented to protect critical areas along the path of these flows. Structural countermeasures could be properly designed if the maximum elevation of the flow and loads acting on the structure are known. In this regard, numerical models could be a very useful tool to predict the design parameters. The multiphase mixture, which is a distinctive feature of these kind of flows, has been frequently

schematized as a single-phase medium with a non-Newtonian behavior and several rheological models, such as power-law [1], Herschel-Bulkley [2], and Bingham [3] models, have been used.

Using the long-wave approximation and assuming laminar flow conditions, numerous studies investigated the characteristics of a wave generated by a sudden release of a finite volume of a non-Newtonian fluid downstream of a gate, both in the absence and in the presence of obstacles [2,4–10]. However, independently of the laminar assumption, the long-wave approximation assumes that the shape of the vertical profiles of velocity and pressure are those pertaining to uniform conditions. Such a hypothesis can fail in a dam break wave, particularly if obstacles are present. Removing the long-wave approximation, the dam break of non-Newtonian fluids has been widely investigated in laminar conditions using both Lagrangian and Eulerian approaches.

In the absence of obstacles, Minussi and de Freitas Maciel [11] simulated a two-dimensional dam break wave of a Herschel-Bulkley fluid propagating on a horizontal plane. In the absence of obstacles, Minussi and de Freitas Maciel [11] simulated a two-dimensional dam break wave of a Herschel-Bulkley fluid propagating on a horizontal plane. The ANSYS CFX software was used, and the fluid-free surface was calculated using the volume-of-fluid [12] (VOF) technique. Waves propagating over an inclined bottom were simulated by Schaer *et al.* [13]. Their study was carried out using the OpenFOAM software with VOF. Simulations of a two-dimensional dam break wave of a Bingham fluid have been performed by Liu *et al.* [14], using the VOF method and discretizing the governing equations through a mixed finite-element and finite-volume method. Both two- and three-dimensional dam break waves of a Bingham fluid have been considered by Valette *et al.* [15]. An adaptive stabilized finite-element technique along with the level set method [16] was used to reproduce the viscoplastic fluid-air interface. The incompressible smoothed particle hydrodynamics (SPH) method was used by Shao and Lo [17] to simulate two-dimensional dam break waves of non-Newtonian fluids described by Cross model rheology [18].

Without using the long-wave approximation, the dynamics of a laminar dam break wave interacting with obstacles were also investigated in both Lagrangian and Eulerian frameworks. For instance, Laigle and Labbe [19] developed a weakly compressible SPH method to simulate the interaction of a dam break wave of a Herschel-Bulkley fluid with a rigid obstacle. Zhou and Sun [20] used a *B*-spline material point method to discretize and solve the Navier-Stokes equations to simulate the impact against a vertical wall of a non-Newtonian wave containing a power-law fluid. Tang *et al.* [21] used finite differences and a two-step projection method to solve the discretized two-dimensional (2D) Navier-Stokes equations to study a dam break wave impacting a vertical obstacle.

Based on the available literature, one can conclude that both Lagrangian and Eulerian (combined with the VOF technique) approaches allow to correctly reproduce the dynamics of a laminar dam break wave of non-Newtonian fluids, even in the presence of obstacles. However, at field conditions, most of these flows are turbulent or weakly turbulent [22].

In the case of wall-bounded shear flows, it is widely accepted that direct numerical simulation (DNS) and large eddy simulation (LES) are valid alternatives to the Reynolds-averaged Navier-Stokes (RANS) equations even for non-Newtonian fluid flows [23–26]. In DNS, no turbulence model is used, and the simulation should capture all eddies up to the dissipative range. In LES the energetically important eddies are resolved and only the smallest turbulent scales are modeled using a subgrid-scale (SGS) turbulence model. Focusing on the study of the interaction of a dam break wave with an obstacle, though DNS is a powerful tool to understand the physics of turbulent non-Newtonian fluids, the LES approach is in many cases preferable because of its reduced computational cost. When applying the spatial filter to the Navier-Stokes equations of non-Newtonian viscous fluids, additional terms are present [25]. However, almost all LES studies have incorporated standard Newtonian dynamic SGS models [27], therefore ignoring the extra terms due to the viscosity fluctuations. This conclusion applies, in particular, to simulations involving power-law fluids [28].

The present study investigates the interaction of a dam break wave of mud with a rigid vertical wall. Eddy resolving numerical techniques are used to account for turbulence effects. The considered mud is a mixture of clay and water whose rheological behavior is described by a shear-thinning

power-law model [1]. With reference to a laboratory setup, four values of the clay concentration (one of these corresponds to the limiting case of a clear water fluid) and two different initial flow depths have been considered. The variation of the clay concentration value allows us to investigate different shear-thinning fluids. For one case, scale effects have been studied by increasing the dimensions of the setup by a factor of 10. The focus is on the cases with non-Newtonian fluids but results are also included for the limiting case of a Newtonian fluid (water) to understand better the effect of flow rheology on the propagation of the dam break wave and its interaction with the endwall and also for additional validation of the numerical model.

A series of 3D numerical LESs simulations with a dynamic Smagorisky model [27] have been carried out. The study is performed using a viscous solver, which is able to account for the power-law rheology and to model the free surface dynamics using the VOF technique. The dynamic Smagorisky model has the advantage that it remains accurate in flows where some regions are nonturbulent. As far as the water is concerned, the solver was shown to accurately predict unsteady free surface flows in RANS simulations including the propagation of dam break waves of water in channels and its interaction with obstacles (e.g., [29,30]). The LES module was validated for wall-bounded and (open channel) free surface flows by Lazzarin *et al.* [31], Wu and Constantinescu [32], Wu *et al.* [33], and Marschall *et al.* [34]. As part of the present study, additional validation simulations were conducted for dam break waves in both turbulent (Newtonian fluid) and laminar (power-law fluid) flow conditions. These validation simulations are directly relevant to the types of flows investigated in the present study. The main goal of the study is to explore the influence of varying clay concentrations of the non-Newtonian fluid and initial flow depth on the front propagation and on the force acting on the vertical endwall. Moreover, the presence of large-scale coherent structures close to the wave front and the free surface (e.g., lobe, clefts, interfacial vortices) and near bed streaks is investigated.

The structure of the paper follows. The numerical model and test cases are described in Sec. II. Validation of the solver for Newtonian and non-Newtonian dam break flows is reported in Sec. III. Section IV discusses the effects of the rheology, of the initial depth of lock fluid, and of the test scale on the evolution of the dam break wave and its interaction with the vertical endwall. Section V presents some final discussion and conclusions.

II. TEST CASES AND NUMERICAL MODEL

A. Test cases

Six test cases are performed, reproducing small-scale dam break waves of non-Newtonian fluids impacting against a vertical wall. An additional test, named case 0, is conducted with a Newtonian fluid (water). The geometry reproduces laboratory experiments carried out with water in a channel 2.92 m long, 0.4 m wide, and 0.5 m high [35]. The channel is divided into two regions by a lock gate situated at $x = 0$ (Fig. 1). A region of length $L_1 = 1.5$ m contains the initial lock fluid with the floodable area on the right of the lock gate. A 0.025-m-high embankment of length $L_2 = 1.36$ m is placed inside the floodable area. The distance between the lock gate and the embankment is $L_3 = 0.015$ m. A short transition region with a slope $\Theta = 45^\circ$ is present at the upstream end of the embankment.

The non-Newtonian fluids considered in the simulations are characterized by a power-law rheology. Assuming a purely sheared unidirectional flow, the shear stress is $\tau = k(\frac{du}{dz})^n$, where k is the consistency index, n is the power-law index, and $\frac{du}{dz}$ is the velocity derivative in the z direction. The power-law relationship of Ng and Mei [1] was used to relate the rheological parameters to the clay concentration (i.e., $k = 1.86 \times 10^{-4} C^{4.45}$, $n = 5.86 C^{-1.34}$, where C is the volume concentration of clay in water). Three different concentrations that are characteristic of those encountered in hyperconcentrated rivers [36,37] and mud flows [38] were considered, $C1 = 4\%$, $C2 = 6\%$, and $C3 = 8\%$, and the corresponding values of the consistency, power-law exponent, and density are reported in Table I.

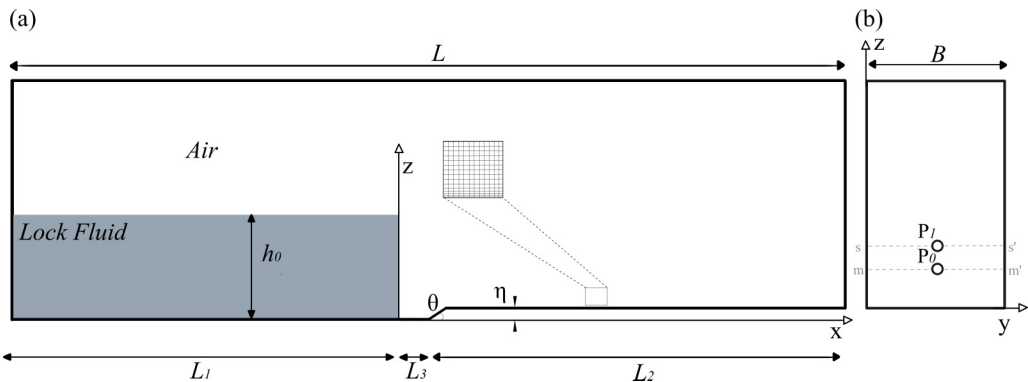


FIG. 1. Sketch of the computational domain. (a) Lateral view of the channel in the x - z plane showing the initial location and depth, h_0 , of the lock fluid. (b) Frontal view showing the endwall. The pressure is sampled at two points situated on the same vertical axis. For cases 0 to 6, the point P_0 is placed at 0.01 m from the channel bottom and point P_1 at 0.03 m.

To evaluate the mixture density ρ the following values of the kaolin clay and water were assumed: $\rho_{kc} = 2600 \text{ kg/m}^3$ and $\rho_w = 1000 \text{ kg/m}^3$. In what follows, γ denotes the specific weight of the fluid. The performed tests are summarized in Table II. In the clear water (CW) case (case 0), the viscosity is assumed to be $\mu = 0.0009 \text{ Pa s}$. For each value of the clay concentration, simulations were conducted with two initial flow depths ($h_0 = 0.2 \text{ m}$ and $h_0 = 0.3 \text{ m}$) of the lock fluid (cases 1 through 6 in Table II). An additional simulation (case 7) was performed with the geometry of case 3 scaled by a factor of 10. Comparison of these two cases allows for estimating scale effects.

In what follows, the results will be presented in dimensionless form. Denoting with g the gravitational acceleration, the reference length, time, and velocity scales are h_0 , $t_0 = \sqrt{h_0/g}$, and $U_0 = \sqrt{gh_0}$, respectively.

The generalized reference Reynolds number can be defined as follows [1]:

$$\text{Re} = \frac{\rho U_0 h_0}{\mu_0} = \frac{\rho U_0^{2-n} h_0^n}{k}, \quad (1)$$

where $\mu_0 = k(\frac{U_0}{h_0})^{n-1}$ denotes the reference viscosity for power-law fluids, while in the clear water case μ_0 denotes the (water) viscosity.

With reference to uniform conditions in a wide channel, i.e., two-dimensional steady parallel flow conditions, one can define the Reynolds number Re with the uniform flow depth h_u and the corresponding depth-averaged velocity U_u . In this case, the critical stability condition of the laminar flow is [1]

$$\text{Re}_c = 0.125 \frac{(1+3n)^n}{2n} [2100 + 875(1-n)]. \quad (2)$$

TABLE I. Rheological parameters.

Fluid	C (%)	k [(Pa s) n]	n	ρ (kg/m 3)
PL1	4	0.09	0.91	1064
PL2	6	0.54	0.53	1096
PL3	8	1.94	0.36	1128

TABLE II. Main parameters of the test cases: β represents the power-law exponent in the equation that correlates the nondimensional front position and the nondimensional time, before the front reaches the downstream vertical wall.

Case	Fluid	k [(Pa s) ^{n}]	n	ρ (kg/m ³)	μ_0 (Pa s)	h_0 (m)	Re	Re _{c}	β
0	CW	0.0009	1	1000	0.0009	0.2	310 000	2100	1.33
1	PL1	0.09	0.91	1064	0.073	0.2	5757	523	1.17
2	PL1	0.09	0.91	1064	0.075	0.3	10386	523	1.24
3	PL2	0.54	0.53	1096	0.184	0.2	2362	504	1.18
4	PL2	0.54	0.53	1096	0.202	0.3	3946	504	1.24
5	PL3	1.94	0.36	1128	0.447	0.2	999	487	1.17
6	PL3	1.94	0.36	1128	0.509	0.3	1613	487	1.25
7	PL2	0.54	0.53	1096	0.316	2	43486	504	1.32

Although Eq. (2) is strictly valid for uniform flow conditions, the Re _{c} value is assumed to be fairly representative of critical conditions even for dam break flows. The values of Re and Re _{c} for each case are also included in Table II.

B. Numerical model

A layer of air was present in the upper part of the computational domain (Fig. 1). The governing equations are the (filtered) Navier-Stokes equations and the advection equation for the volume fraction of water, α , that is used to track the interface between the wave fluid and the surrounding air domain in the VOF LESs. In the VOF approach, one tracks (wave) fluid volume rather than fluid surfaces (e.g., the interface between the wave fluid and the air). So, there is no need to explicitly model shear at the interface between the air and the wave fluid. In this approach, the same equations are solved inside the air and wave fluid subdomains, and the same turbulence model is used over the whole computational domain. The air is treated as a standard incompressible Newtonian fluid. The filtered continuity and momentum equations are

$$\frac{\partial u_j}{\partial x_j} = 0, \quad (3)$$

$$\rho \frac{\partial u_i}{\partial t} + \rho \frac{\partial u_i u_j}{\partial x_j} = -\frac{\partial p}{\partial x_i} + \frac{\partial}{\partial x_j} \left[\mu \left(\frac{\partial u_i}{\partial x_j} + \frac{\partial u_j}{\partial x_i} \right) \right] + g \delta_{i,3} - \sigma_{ij}, \quad (4)$$

where p and u_i represent the dimensional filtered pressure and Cartesian velocity i component, respectively. In Eq. (4), $\delta_{i,k}$ denotes the Kronecker delta function and x_1, x_2 , and x_3 the x, y , and z variables, respectively. Assuming a power law as the constitutive relation, the viscosity is

$$\mu = k (S_{ij} S_{ij})^{\frac{n-1}{2}} \quad (5)$$

with S_{ij} the filtered velocity deformation tensor:

$$S_{ij} = \frac{1}{2} \left(\frac{\partial u_i}{\partial x_j} + \frac{\partial u_j}{\partial x_i} \right). \quad (6)$$

The subgrid stress tensor σ_{ij} is related to the filtered velocity deformation tensor S_{ij} as follows [24]:

$$\sigma_{ij} = -2\mu_t S_{ij} = -2C_d \Delta^2 |S| S_{ij}, \quad (7)$$

where μ_t is the turbulent dynamic viscosity, Δ is the local grid size, and C_d is the model parameter that is dynamically determined [39]. The SIMPLE (Semi-Implicit Method for Pressure Linked Equations) algorithm is used to integrate the discretized Navier-Stokes equations that are advanced

in time using a semi-implicit, iterative method. The advective terms in the momentum equations are discretized using a third-order, monotonic scheme that blends an upstream-centered scheme (MUSCL) with the central-differencing scheme in the LESs. The diffusive and pressure gradient terms are discretized using the second-order, central-differences scheme. The implicit temporal discretization is also second-order accurate. Due to the nonlinear nature of the problem for both the convective and diffusive terms, an iterative solution is required. The resulting linear system is solved using Algebraic Multigrid (AMG). The air-fluid interface is modeled using an algebraic VOF approach. The VOF free surface tracking technique has been successfully applied to simulate a dam break and flood-wave problem [11,30,40–43]. A pure-advection equation is solved for the volume fraction of water (α) over the whole computational domain:

$$\frac{\partial \alpha}{\partial t} + u_j \frac{\partial \alpha}{\partial x_j} = 0. \quad (8)$$

In cells containing only water, $\alpha = 1$, while in cells containing only air, $\alpha = 0$. A value of $\alpha = 0.5$ has been chosen to visualize the interface and determine the front position. To maintain a sharp interface, a high-resolution interface capturing scheme was employed [44].

A pressure outlet boundary condition with a zero volume fraction of the liquid phase and a pressure of 0 Pa was specified at the top boundary. At all the other boundaries, no-slip conditions (zero velocity) were imposed. The initial velocity field was set to zero and the lock gate was removed instantaneously at $t = 0$. The time step was fixed for all simulations and it has been estimated such that the Courant number is close to 0.2. The instantaneous pressure distribution on the endwall was used to estimate the impact force once the wave reached the endwall. The level of mesh refinement was finer in regions situated close to the channel bottom, lateral walls, and endwall, such that the attached boundary layer and the velocity gradients were well resolved. The Cartesian-like, unstructured mesh was refined near these two boundaries using seven prism layers. This allowed us to place the first point off the wall surface at about 0.0002 m (i.e., one wall unit) [30,43,45–47].

Away from the endwall and lateral walls, the spanwise and streamwise grid was about 20–30 wall units. The total number of cells was close to 1.8×10^7 in case 1 through case 6 simulations. Due to the higher Reynolds number, the number of prism layers was increased up to 15 in the case 0 and case 7 simulations such that the first grid point off the two wall surfaces was situated at about one wall unit. This also allowed avoiding the use of wall functions in the LES simulations.

The simulations were run on the Argon HPC computer at the University of Iowa using 28 nodes of 4 GB of RAM per core. The physical time required to complete one simulation was on the order of two weeks.

A grid sensitivity analysis was conducted. As shown in Fig. 2 for case 1, the computed time histories of the impact force (for unit width) are close in the simulations conducted with meshes containing 1.8×10^7 and 3.0×10^7 cells. In particular, the peak value of the nondimensional impact force is about 0.6 in both cases. Moreover, the temporal evolution of the front position was basically identical in the two simulations [e.g., see Fig. 2(b)]. Based on these results it can be concluded that the simulations performed on the grids containing around 1.8×10^7 cells capture with sufficient accuracy the variation of the quantities of engineering interest (e.g., impact forces and front position).

III. MODEL VALIDATION

A. Turbulence model validation

The water dam break experiment carried out at the Hydraulic Laboratory of the University of Naples “Federico II” in the setup of Fig. 1 has geometrical and flow parameters reported in Table II as case 0. The free surface evolution is recorded by two high-speed charge coupled device cameras that are horizontally aligned. Methylene blue is dissolved in water to improve the readability of the experimental image. The postprocessing of the images allows for obtaining bidimensional free surface profiles and the water front celerity. The pressure on the endwall is recorded by means of

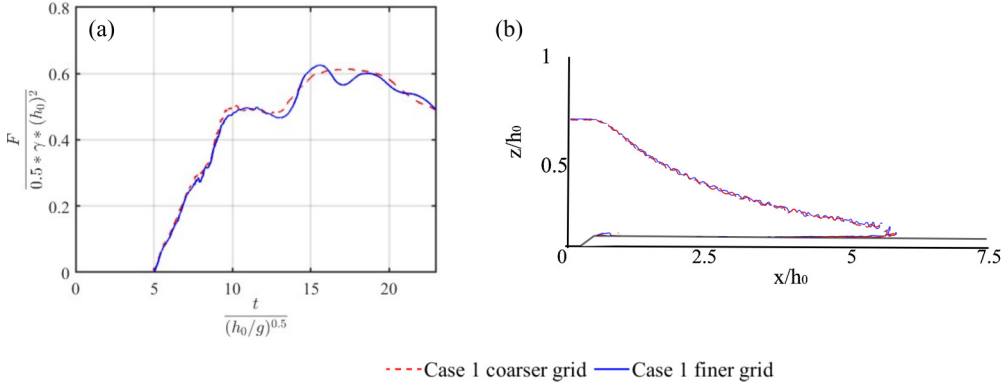


FIG. 2. Grid dependency study for case 1. (a) Temporal variation of the nondimensional impact force $F/0.5\gamma(h_0)^2$; (b) wave free surface at $t/t_0 = 4.3$. The finer grid contains 3.0×10^7 cells and the coarser grid contains 1.8×10^7 cells.

nine pressure transducers uniformly distributed every 0.02 m along the vertical centerline of the channel and the force is obtained by integrating their measurements. Additional details concerning the experimental setup and the measurement techniques can be found in Ref. [35]. The flow inside the water dam break wave is turbulent.

Figure 3 compares the simulated and measured longitudinal flow profiles at different time instants, while Fig. 4 reports the time history of the pressure and impact force on the endwall.

The numerical simulation accurately captures the shape of the wave and the location of the front (e.g., see results for $t/t_0 = 2.9$ in Fig. 3), which means it correctly predicts the water wave celerity, during the propagation before the arrival to the endwall. Once the wave reaches the endwall, a thin jetlike flow forms parallel to the endwall. The maximum runup of the wave on the vertical endwall is reached around $t/t_0 = 6.4$ in both simulation and experiment (Fig. 3). As the thin layer of water moving upwards decelerates due to gravity, the thickness of the layer of water parallel to the endwall increases, while the wave penetration height remains about the same. Moreover, the head of this region containing water starts rolling to form a vortex (e.g., see results for $t/t_0 = 7.9$ in Fig. 3) and a backward-propagating bore starts forming. The simulation accurately predicts the position of the front of this bore (e.g., see results for $t/t_0 = 15$ in Fig. 3 where the bore position is located at $x/h_0 \approx 3.8$). Moreover, the simulation reproduces the overall shape of the domain containing water once the backward-propagating bore forms and a thick layer is present where the air is entrained inside the bore fluid propagating on top of the bottom layer of water moving toward the endwall.

The simulation successfully predicts some important phenomena observed in the experiment that include air entertainment, the breaking of the sheet of vertical water into bubbles, and the formation of pockets of air inside the top layer containing backward-propagating fluid once the bore forms (Fig. 3). This is made possible by the sharp interface treatment used in the VOF module of the viscous flow solver. Overall, the simulation accurately captures the front position and wave celerity before the wave reaches the endwall, as well as the bore position and bore celerity at later times.

The other critical element in assessing the accuracy of the numerical model is its capacity to predict the temporal evolution of the pressure on the endwall and, ultimately, the magnitude of the impact force on it. Figure 4(a) shows that the model accurately captures the peak value of the pressure at the bottom of the endwall as the thin front of the wave reaches the wall around $t/t_0 = 5$, followed by the subsequent increase and decrease of the pressure associated with the formation of the backward-propagating bore for $t/t_0 > 10$. The pressure temporal variation is also accurately captured at point *P1* situated at a higher elevation, both during the formation of the thin layer of water parallel to the endwall, when a first peak is reached, and, then, once the bore starts forming. Comparison of the numerical and experimental predictions of the impact force shows a similar level

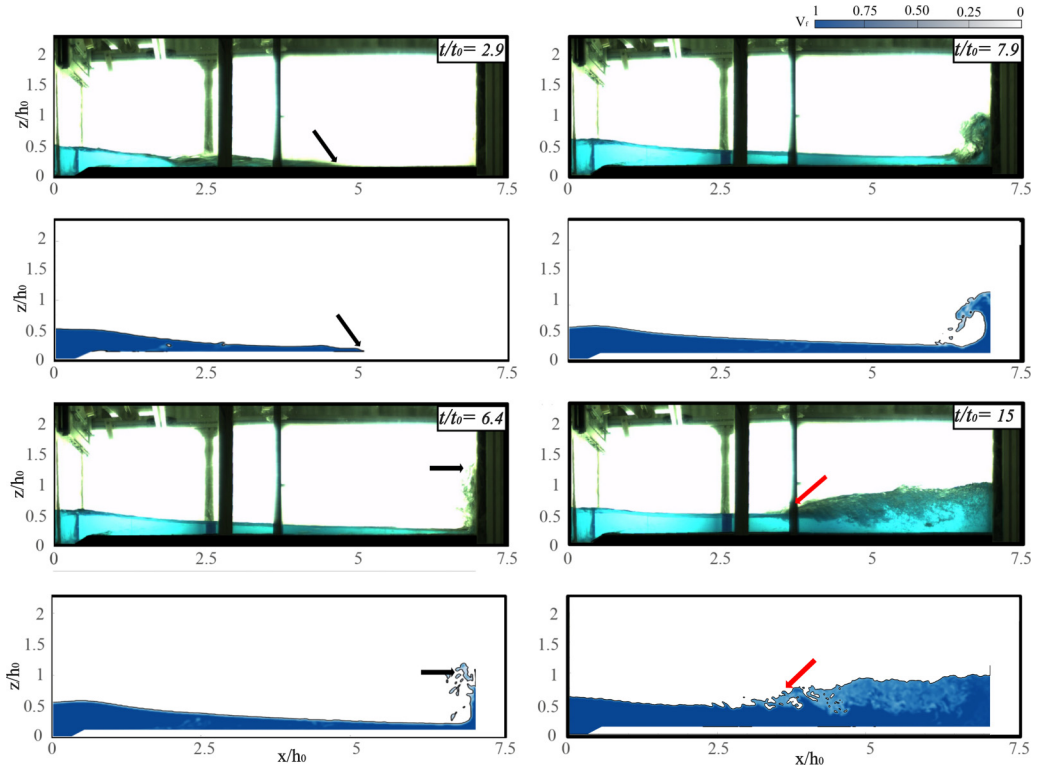


FIG. 3. Dam break wave evolution in case 0 ($h_0 = 0.2$ m) at four time instances. Methylene blue is dissolved in water to improve the readability of experimental images. The bottom frames show the volume fraction predicted by LES. The black arrow shows the front position, while the red arrow shows the front of the backward-propagating bore.

of agreement to that observed for the pressure time histories. Though there is some disagreement in terms of the local oscillations, the variation of the total impact force is well captured by the simulation not only in terms of the peak value (less than 3% difference with experimental value) and the time to peak ($t/t_0 = 15$ – 16), but also in terms of its temporal variation. The peak value is recorded way after the backward-propagating bore forms (see results for $t/t_0 = 15$ in Fig. 3), just before the water level on the endwall starts to decay slowly.

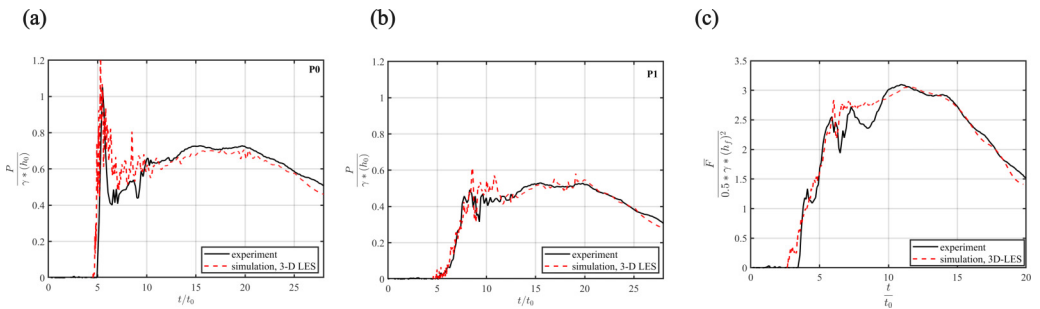


FIG. 4. Time histories of the measured (black line) and predicted (red line) nondimensional variables for case 0: (a) pressure at point P_0 , (b) pressure at point P_1 , and (c) impact force acting on the endwall.

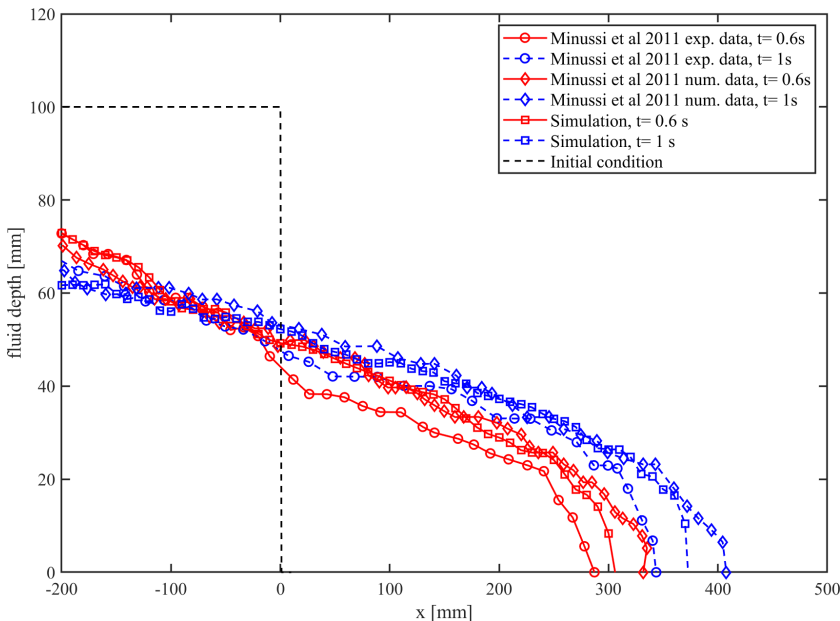


FIG. 5. Temporal evolution of the flood wave corresponding to the experiment of Minussi and de Freitas Maciel [11]. Present LES predictions at $t = 0.6$ s and $t = 1.0$ s are compared with the experiment and simulation results reported by Minussi and de Freitas Maciel [11]. The black dashed line shows the domain containing non-Newtonian fluid at $t = 0$ s.

B. Non-Newtonian validation

Validation simulations for a dam break wave containing a non-Newtonian fluid were performed for the experiments reported by Minussi and de Freitas Maciel [11]. In this experiment, a rectangular volume of Hershel-Bulkley fluid was released at $t = 0$ in a smooth-bed channel. Besides the experimental data and present LES data, results are also included for a laminar-flow simulation conducted by Minussi and de Freitas Maciel [11] using a Navier-Stokes solver with VOF. Figure 5 compares the flow depth profiles at two time instants. Though both simulations slightly overestimate the wave front celerity (the error is by about 50% lower in the present simulation; e.g., see front position in Fig. 5), the shape of the dam break wave is well captured. One should mention that for the flow conditions in this test case, the eddy viscosity values predicted in the LES are very low, so turbulence effects are negligible.

IV. RESULTS

Given that the present simulations are conducted in three dimensions, with the lateral sidewalls of the channels part of the computational domain, it is relevant to discuss the presence of 3D effects. Due to the limited length of the initial volume of lock fluid, the discharge moving past the gate position ($x = 0$) is not expected to remain constant, especially in the later stages of the dam break flow, after the backward-propagating lock current reflects at the left wall and the forward-moving bore passes the gate. Indeed, results in Fig. 6(a) for cases 0, 1, 3, and 5 ($h_0 = 0.2$ m) confirm that the volumetric discharge decreases fairly monotonically with time in these simulations for $t/t_0 > 5$, which is also the approximate time when the front reaches the endwall. However, in a fairly good approximation one can consider the lock fluid discharge at the gate to remain constant starting a short time after the gate is released and until the front wave reaches the endwall. This time period is referred to in the present study as the propagation phase.

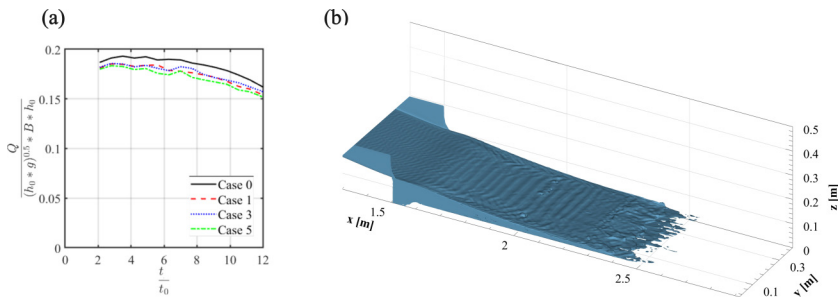


FIG. 6. General features on the flow generated by the release of the lock fluid. (a) Volumetric flux of lock fluid at the lock gate ($x/h_0 = 0$). (b) Shape of the interface between the fluid and the air ($\alpha = 0.5$ and $t/t_0 = 2.9$) for case 1, showing the nonuniformity of the front position in the spanwise direction.

Analysis of the results for all non-Newtonian cases shows that 3D effects are very mild over most of the dam break wave except near its front. The boundary layers forming at the two sidewalls have a very local effect on the velocity field, with the streamwise velocity remaining fairly uniform in the spanwise direction, outside of the boundary layers. In the simulations performed with non-Newtonian fluids, some instabilities develop in the streamwise direction along the interface between the wave fluid and the air, but they are basically two dimensional. They can be observed in Fig. 6(b), which visualizes the 3D interface between the lock fluid and the air for case 1. Meanwhile, the front position is characterized by a large degree of nonuniformity in the spanwise direction and 3D instabilities develop near the front of the wave. These instabilities are similar to the lobe-and-cleft instabilities observed at the front of lock-exchange turbulent gravity currents [48–50]. Lobelike instabilities were also observed to form at the front of dam break water waves at high Reynolds numbers [30]. So, the front instability appears to be a general characteristic of dam break flows that are not limited to Newtonian fluid and high Reynolds numbers.

The experiments of gravity currents by Simpson [51] indicate the following empirical relationship for the lobes' width [49]:

$$\frac{b}{d} = 7.4\text{Re}_f^{-0.39}, \quad (9)$$

where b is the mean lobe size, d is the front head height of the gravity current, $\text{Re}_f = \frac{u_f d}{\nu}$ is the front Reynolds number, and u_f is the velocity of the front. These formulas were developed based on experiments for high-Reynolds-number gravity currents where the height of the raised head is almost constant. In the present dam break flow, the depth of the wave decreases monotonically to zero at the front. Then, for testing the validity of Eq. (9) for dam break flows, the reference length is assumed to be half of the initial depth: $h_0/2$. For example, Simpson's [51] formula predicts for case 1 at $t/t_0 = 2.9$ [Fig. 6(b)] $b/B = 0.09$, which is just 8.3% greater than the value inferred from our numerical simulation. This indicates that the correlations obtained for Newtonian gravity currents still seem to apply even for non-Newtonian dam break flows, suggesting that the mechanisms for the formation of these structures near the front are similar.

The following two sections investigate the effects of fluid rheology and initial depth of the lock fluid on turbulence, front evolution, bed shear stresses, and impact force on the endwall. Scale effects are also analyzed in the last section. The goal is to understand if the behavior of a dam break wave containing a non-Newtonian fluid changes once the Reynolds numbers are sufficiently high for turbulence to play a larger role compared to flow conditions observed in typical laboratory-scale investigations of these flows.

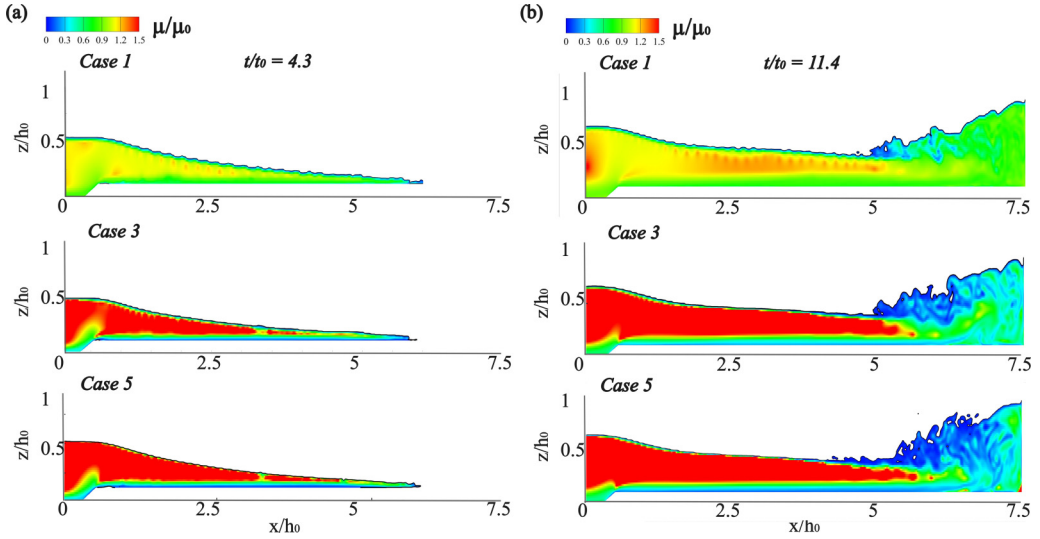


FIG. 7. Effects of rheology on the nondimensional viscosity for simulations in cases 1, 3, and 5 at two nondimensional times. (a) Propagation phase, (b) impact phase.

A. Effects of rheology

The rheology effect is investigated by comparing the results of cases 1, 3, and 5 having the same initial depth $h_0 = 0.2$ m. When relevant, results of the Newtonian fluid case (case 0) are also included.

1. Viscosity field

For non-Newtonian fluids, the viscosity is a field function that depends on the velocity gradients [see Eq. (5)]. As shown in Table II, increasing the clay concentration C enhances the consistency index k and reduces the power-law exponent n . As the viscosity is directly proportional to k , viscosity increases with increasing C . On the other hand, for shear-thinning ($n < 1$) non-Newtonian fluids, viscosity decreases in regions where velocity gradients are high and increases in regions where the velocity field is fairly uniform.

Figure 7 compares the distributions of the nondimensional viscosity μ/μ_0 along the middle vertical plane of the channel at two times for cases 1, 3, and 5 (Table II), corresponding to an increasing concentration C (i.e., with increasing k and decreasing n values). As exemplified in Fig. 7(a) ($t/t_0 = 4.3$), two regions can be identified inside the dam break wave during the propagation phase ($t/t_0 < 5$): the core zone and the shear zone. The velocity gradients are low inside the core zone. So, if the concentration C increases, the nondimensional viscosity increases too. Inside the shear zone, close to the bed and the free surface, the increase of the concentration C leads to a decrease of μ/μ_0 . During the impact phase ($t/t_0 > 5$), the nondimensional viscosity field shows the same pattern as observed during the propagation phase up to the front of the backward-propagating bore [e.g., see Fig. 7(b) for $t/t_0 = 11.4$]. In between the vertical endwall and the front of the backward-propagating bore, a mixing layer develops. Due to the high shear between the bore and lower layer of downstream moving wave fluid, a zone of low μ/μ_0 forms. The average nondimensional viscosity values inside this region are decaying with increasing concentration C .

2. Front propagation

For all cases, the relationship between the nondimensional front position and the nondimensional time follows a power law, $x_f/h_0 \sim (t_f/t_0)^\beta$, with $\beta > 1$. The values of β are included in Table II.

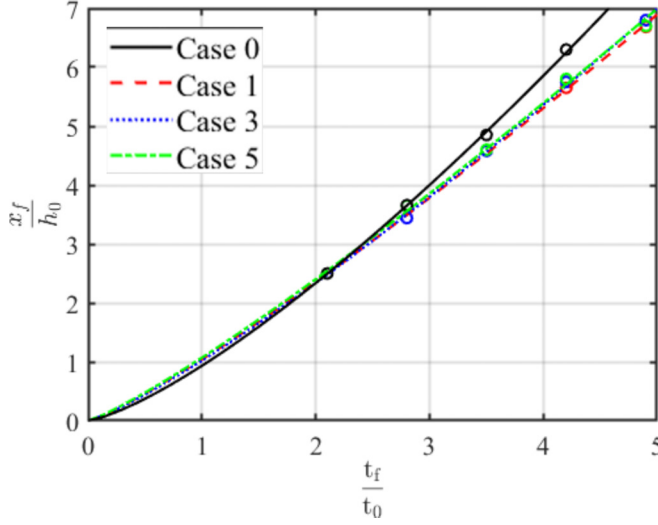


FIG. 8. Effects of rheology on the temporal variation of the nondimensional front position, x_f/h_0 , in the case 0, case 1, case 3, and case 5 simulations.

Figure 8 compares the temporal variations of x_f/h_0 for the cases with $h_0 = 0.2$ m. Even for the low-concentration case 1 ($C = 4\%$), the presence of solid material induces an increase of the viscosity by at least two orders of magnitude with respect to the clear water case (case 0). As a result, the front celerity for the non-Newtonian cases in Fig. 8 is lower compared to case 0 for $t/t_0 > 2$. The temporal variations of the front position and the values of β in the three non-Newtonian fluid simulations are quite close and about 15% lower than the value estimated in case 0. It is possible that some differences in β may be observed in a longer channel between cases with different values of the concentration C .

3. Bed shear stress

The bed shear stress longitudinal distributions, reported in Fig. 9(a) for the cases with $h_0 = 0.2$ m, have been calculated using the streamwise velocity values at the first grid point off the channel bed and nondimensionalized by $\tau_0 = (\rho_s - \rho)gd$, where the assumed particle diameter was $d = 0.005$ m and its density $\rho_s = 2700$ kg/m³. For non-Newtonian fluids, the bed shear stress is

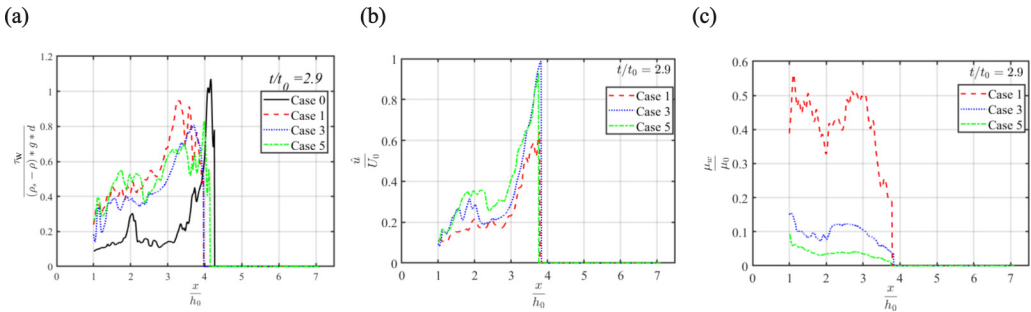


FIG. 9. Effects of rheology on the bed shear stress and related variables in the case 0, case 1, case 3, and case 5 simulations: (a) nondimensional bed shear stress, τ_w/τ_0 ; (b) nondimensional streamwise velocity component at the first grid point off the bed surface, \hat{u}_1/U_0 ; and (c) nondimensional viscosity, μ_w/μ_0 . Results are shown at $t/t_0 = 2.9$.

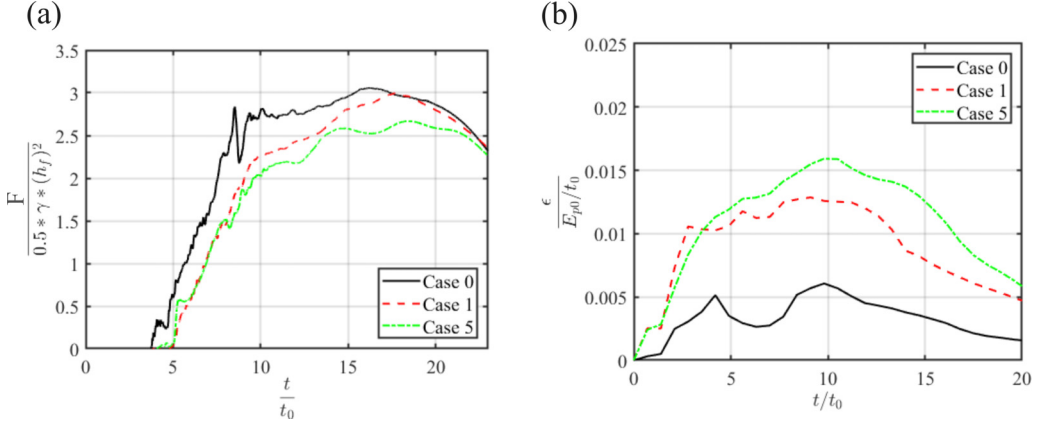


FIG. 10. Effects of rheology on the temporal variation of the nondimensional impact force on the endwall and on the total nondimensional dissipation rate for the case 0, case 1, and case 5 simulations. (a) $F / (0.5\gamma h_f^2)$; (b) $\epsilon / (E_{p0}/t_0)$.

a nonlinear function of the velocity gradient at the bed surface and the rheological parameters k and n . Since the streamwise velocity component is about two orders of magnitude larger than the other two components, the effects of the velocity gradient on the bed shear stress can be assessed based on the distribution of the streamwise velocity component at the first grid point off the bed surface (\hat{u}_1).

Results in Fig. 9(b) show an overall increase of \hat{u}_1 with increasing clay concentration, especially just behind the front of the wave. Meanwhile, the bed viscosity (μ_w / μ_0) decreases monotonically with increasing clay concentration [Fig. 9(c)], in part due to the increased velocity gradient inside the near-bed shear-dominated zone. For this reason, the average value of μ_w / μ_0 is about five times larger in case 1 compared to case 5 [Fig. 9(c)]. Due to the shear-thinning nature of the flow, the bed viscosity starts decreasing near the front of the wave. At $t/t_0 = 2.9$ inertial effects are still significant inside the dam break wave, which explains why the differences in the near-bed velocities are not very large among the three cases shown in Fig. 9(b). One should also note that, even if the viscosity in non-Newtonian fluids is about two orders of magnitude lower with respect to the clear water simulation (case 0), the peak (wave front) value of the bed shear stress in case 0 is comparable to the corresponding values in the non-Newtonian tests. However, the bed shear stress average values over the body of the dam break wave are a couple of times smaller in the case 0 simulation [Fig. 9(a)]. This is mainly because the bed dynamic viscosity and near-bed velocity decrease and, respectively, increase with increasing clay concentration. Thus, the body of the wave containing a non-Newtonian fluid exerts a higher shear on the bed compared to case 0.

4. Forces and energy dissipation

Figure 10 illustrates the temporal variation of the nondimensional impact force exerted on the endwall and the nondimensional total dissipation rate. The latter quantity can explain some of the trends observed in the variation of the impact force. The local (viscous plus SGS) dissipation rate is

$$\hat{\epsilon}(x_1, x_2, x_3, t) = (\mu + \mu_t) S_{ij} S_{ij}, \quad (10)$$

whose volume integral over the flow domain represents the volume-integrated dissipation rate $\epsilon(t)$.

Denoting with E_k the kinetic energy of the fluid and with E_p the work done by external (gravitational) forces on the fluid, both evaluated over the whole flow domain, the following integral

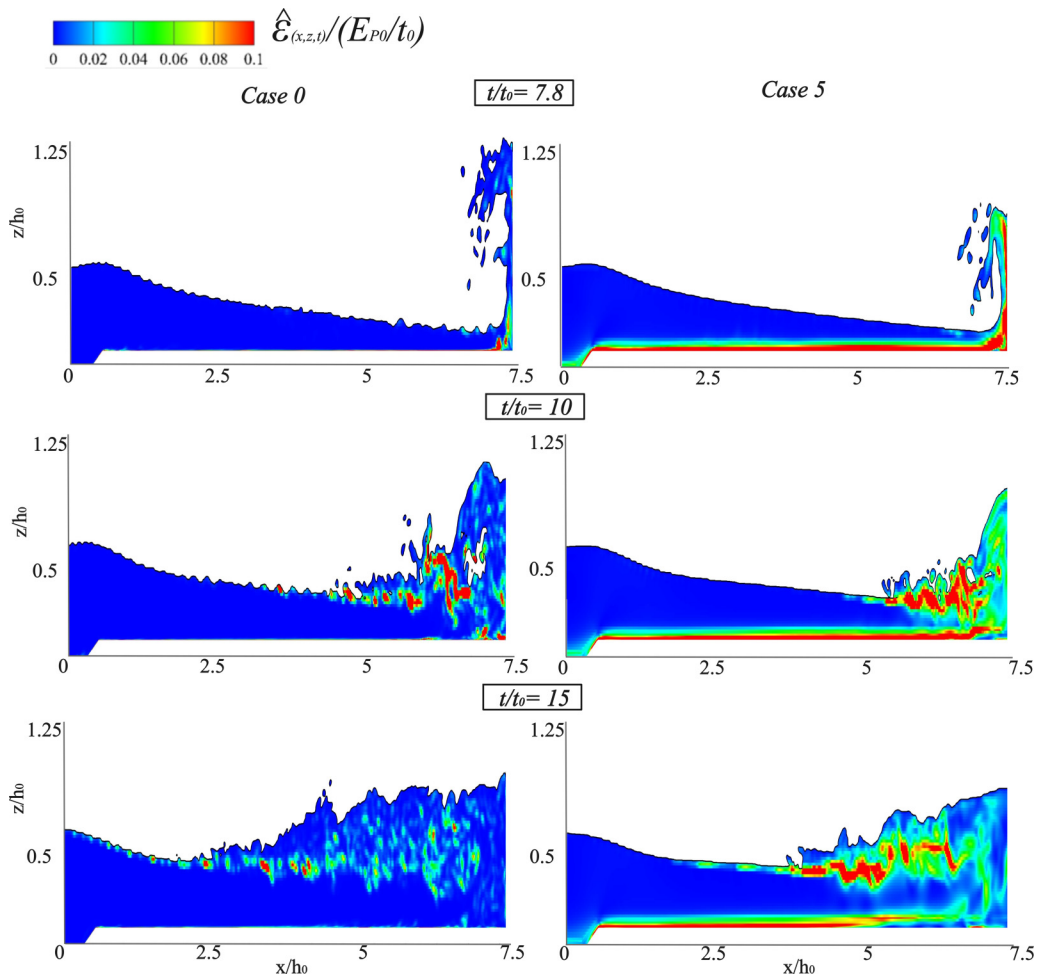


FIG. 11. Distribution of the nondimensional local dissipation rate for the case 0 and case 5 simulations during the impact phase.

conservation law holds [43]:

$$\frac{dE_k}{dt} = -\epsilon(t) - \frac{dE_p}{dt}. \quad (11)$$

In what follows, the terms in Eq. (11) are made dimensionless using the ratio between the initial potential energy and the reference time: E_0/t_0 . The impact force is made dimensionless by dividing by $0.5\gamma h_f^2$, where h_f is the fluid level at the endwall at the end of each simulation, i.e., when the flow is at rest.

Figure 11 compares the spatial distribution of the dissipation rate increases 0 and 5. The dam break wave in the clear water case reaches the endwall earlier ($t/t_0 \approx 4$) compared to the other simulations ($t/t_0 \approx 5$) performed with the same value of h_0 but with a non-Newtonian fluid [Fig. 10(a)]. The slowing down of the wave current is related to the much higher dissipation taking place inside the dam break wave for cases with a non-Newtonian fluid. For example, the dissipation rate at the end of the propagation phase is about two times larger in cases 1 and 5 compared to case 0 [Fig. 10(b)]. The front of the wave as it reaches the endwall is more impulsive in the clear water case, and then the vertical runup height of the jetlike flow forming along the endwall is larger in

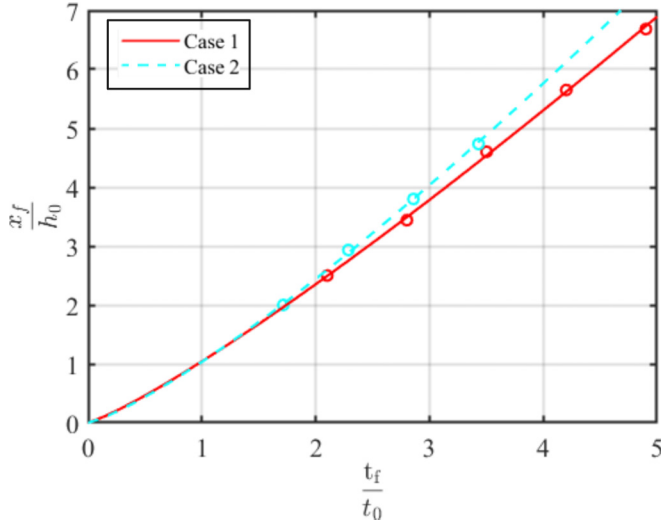


FIG. 12. Effects of the initial depth of the lock fluid on the temporal variation of the nondimensional front position, x_f/h_0 , for the case 1 and case 2 simulations.

case 0 compared to case 5 (see Fig. 11 at $t/t_0 = 7.8$). As the effect of gravity on the evolution of the jetlike flow becomes larger, the jet evolves into a counterclockwise vortex which interacts with the incoming body of the dam break wave (Fig. 11, $t/t_0 = 10$). This interaction is accompanied by the generation of turbulence and strong air entrainment inside the wave fluid situated close to the endwall, especially in case 0. This is consistent with the fact that the impact force in case 0 shows oscillations and irregular pulsations for $8 < t/t_0 < 12$ [see Fig. 10(a)]. On the other hand, the corresponding simulations conducted with a non-Newtonian fluid show a fairly monotonic increase of the impact force during this phase [see the curves for cases 1 and 5 in Fig. 10(a)]. Because viscous effects are stronger, the jet reaches a lower maximum elevation and produces a weaker counter-rotating vortex (e.g., compare results for cases 0 and 5 at $t/t_0 = 7.8$ and 10 in Fig. 11). As a result, the impact force in case 1 and 5 does not display the large oscillations observed in case 0. After $t/t_0 \approx 7.5$, the values of the nondimensional dissipation rate for the case 1 and case 5 simulations start diverging [Fig. 10(b)]. They show an increase of the dissipation with the clay concentration increase. The same pattern can be seen in the behavior of the nondimensional impact force in Fig. 11(a), with the maximum impact force in case 5 being about 15–20% lower than in case 1 for $t/t_0 > 10$. This is mainly due to the increase in the thickness of the shear layer forming in between the backward-propagating bore and the lower-elevation, forward-moving base flow with increasing clay concentration. In all cases, this shear layer region is characterized by high local dissipation rates (e.g., see Fig. 11 for $t/t_0 = 15$).

B. Effects of depth of lock fluid

The effects of increasing the initial depth of the lock fluid on the dam break wave and its capacity to induce bed erosion and forces on the vertical endwall are evaluated based on comparing results of simulations conducted with $h_0 = 0.2$ m and $h_0 = 0.3$ m having the same rheology (case 1 vs case 2, case 3 vs case 4, and case 5 vs case 6). For a given clay concentration the front advances faster with increasing h_0 (e.g., see Fig. 12, which compares results for cases 1 and 2). As for the $h_0 = 0.2$ m simulations, the variation of the front position with time in the $h_0 = 0.3$ m simulations conducted with a non-Newtonian fluid can also be described by a power law, but the predicted value of β is slightly larger ($\beta = 1.25$; see Table II).

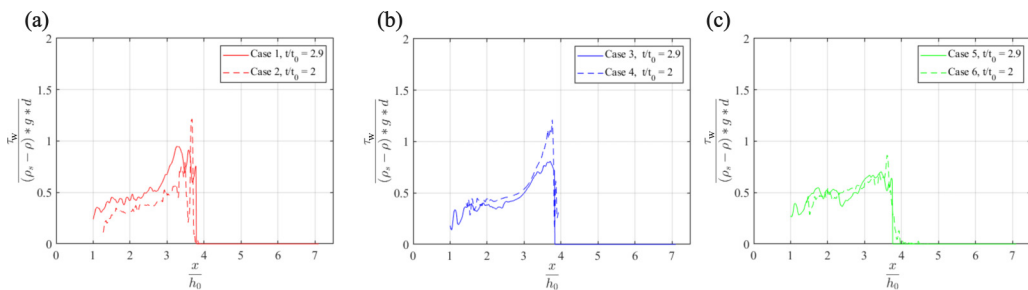


FIG. 13. Effects of initial depth of lock fluid on the nondimensional bed shear stress distributions: (a) cases with $C = 4\%$, (b) cases with $C = 6\%$, and (c) cases with $C = 8\%$. The comparison is shown when $x_f/h_0 = 3.8$.

As shown in Fig. 13, for all clay concentrations, the streamwise distribution of the bed shear stress in the $h_0 = 0.3$ m simulations predicts slightly higher values near the wave front. This is mainly due to the higher front celerity in the simulations conducted with a higher value of h_0 . Meanwhile, the bed shear stress levels are very close over the body of the current in the simulations conducted with $C \geq 6\%$ [Figs. 13(b) and 13(c)]. Increasing the initial depth of the lock fluid makes the dam break wave and its interaction with the endwall more impulsive. Indeed, the comparison between Figs. 10(a) and 14(a) show that the impact forces in case 2 and case 6 simulations performed with $h_0 = 0.3$ m present stronger oscillations compared to those observed in the corresponding (case 1 and case 5) simulations conducted with $h_0 = 0.2$ m. The large oscillations of the impact force in between $t/t_0 = 7$ and $t/t_0 = 12$ for cases 2 and 6 [Fig. 14(a)] are due to the increased vertical penetration distance of the jetlike flow on the endwall. This generates a stronger counter-rotating vortex and increased turbulence in the region where the fluid originating the vortex reaches the forward-propagating wave fluid. The first peak at $t/t_0 \approx 7$ corresponds to the time when the counter-rotating vortex starts detaching from the endwall. The second peak at $t/t_0 = 12$ occurs sometime after the backward-propagating bore forms and the water level at the endwall starts decreasing. The other main effect of increasing h_0 is that it reduces the dependence of the impact force on the clay concentration of the non-Newtonian wave fluid. Indeed, the impact forces in cases 2 and 6 [Fig. 14(a)] are much closer than the impact forces in cases 1 and 5 [Fig. 10(a)]. The temporal histories of the total dissipation rate for cases 2 and 6 in Fig. 14(b) are only mildly dependent on the clay concentration until $t/t_0 \approx 10$. This means that dissipation is mainly determined by velocity

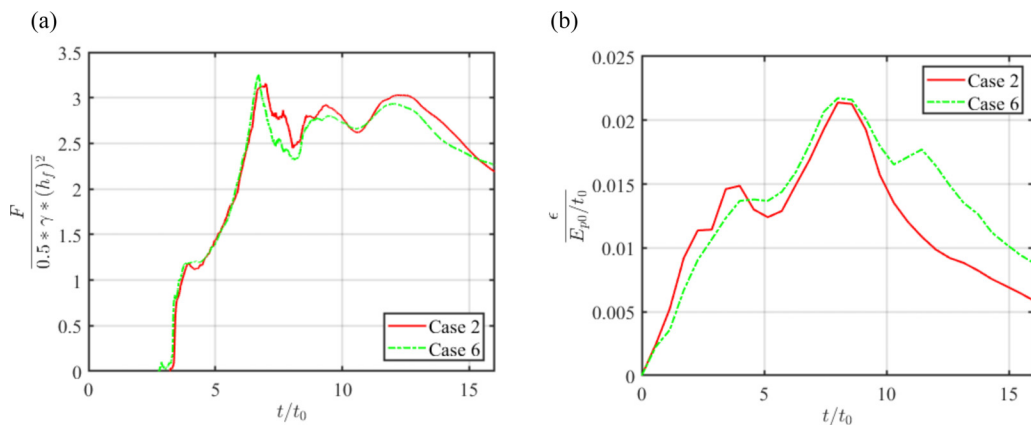


FIG. 14. Temporal variation of the nondimensional impact force acting on the endwall and total dissipation rate simulations conducted with $h_0 = 0.3$ m: (a) $F/(0.5\gamma h_f^2)$, (b) $\epsilon/(E_{p0}/t_0)$.

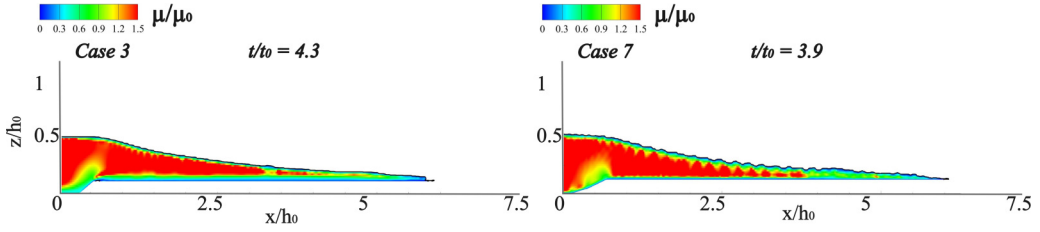


FIG. 15. Scale effects on the nondimensional dynamic viscosity for the case 3 and case 7 simulations.

gradients. As such, it is not surprising that the time series of the impact force in cases 2 and 6 are basically identical until $t/t_0 \approx 10$ [Fig. 14(a)]. At later times, case 6 is more dissipative [Fig. 14(b)], and the impact force in case 6 is slightly smaller compared to case 2 [Fig. 14(a)].

C. Scale effects

Comparison of cases 3 and 7 allows investigating scale effects on non-Newtonian dam break flows and their interaction with a vertical endwall. The two cases have the same rheology (Table II) but the length scale is ten times larger in case 7, which increases the Reynolds number calculated using Eq. (2) from 2.362 in case 3 to 43.486 in case 7. As a result, both inertial and turbulence effects are expected to be significantly stronger in case 7. As the Reynolds number increases, the near-bed velocity gradients increase while the velocity profile becomes more uniform inside the core region situated in between the near-bed shear zone and the interface with the surrounding air.

The comparison of the nondimensional dynamic viscosity distributions for $x_f/h_0 = 6$ in Fig. 15 shows that, away from the front (e.g., for $x/h_0 < 3.75$), the near-bed shear zone in case 7 becomes thinner while the dynamic viscosity increases inside the core region. This is due to the shear-thinning characteristics of the non-Newtonian wave fluid where the decrease of the velocity gradients inside the core region generates an increase of μ/μ_0 . No core region is present in between the front and $x/h_0 = 3.75$. Inside this thin region, the nondimensional dynamic viscosity in case 7 is lower compared to case 3 because of the increase of the streamwise velocity gradients. During the impact phase [e.g., see Fig. 16(b)], the mixing layer forming in between the backward-propagating bore and the lower layer of forward-propagating fluid is thicker in case 7 (compare the elongated region of blue vorticity in Fig. 16). This is accompanied by a large increase of the turbulence between the endwall and the front of the bore, as seen by comparing the nondimensional eddy viscosity values in Fig. 16(c).

Finally, the out-of-plane vorticity fields in Fig. 16(a) show the presence of very energetic eddies in this region, whose average size is significantly smaller than that of the eddies observed in case 3. The increase in the velocity gradients generated by the smaller-scale turbulent eddies also explains why the nondimensional dynamic viscosity levels are smaller in case 7 in between the endwall and the front of the bore [Fig. 16(b)]. As opposed to case 3, some turbulence is also generated along the interfacial region in case 7. So, for such high Reynolds numbers, a laminar 3D model is not expected to be very accurate even for non-Newtonian dam break flows. As expected, increasing the Reynolds number leads to stronger inertial effects. As a result, the front celerity is larger in case 7 compared to case 3, as observed from Fig. 17 where, at all times, the front traveled a longer distance in case 7 compared to case 3. The value of the power-law constant also increases from 1.18 to 1.32 (Table II).

The other important effect of the increased front celerity is the much larger amplification of the bed shear stress for some distance behind the front (assuming the same particle diameter d of the small-scale tests for τ_0 calculation). For example, for $x_f/h_0 = 3.8$, the peak bed shear stress at the front of the wave is about three times larger in case 7 compared to case 3 and the region where the bed shear stresses are affected by the Reynolds number extends for about h_0 behind the front

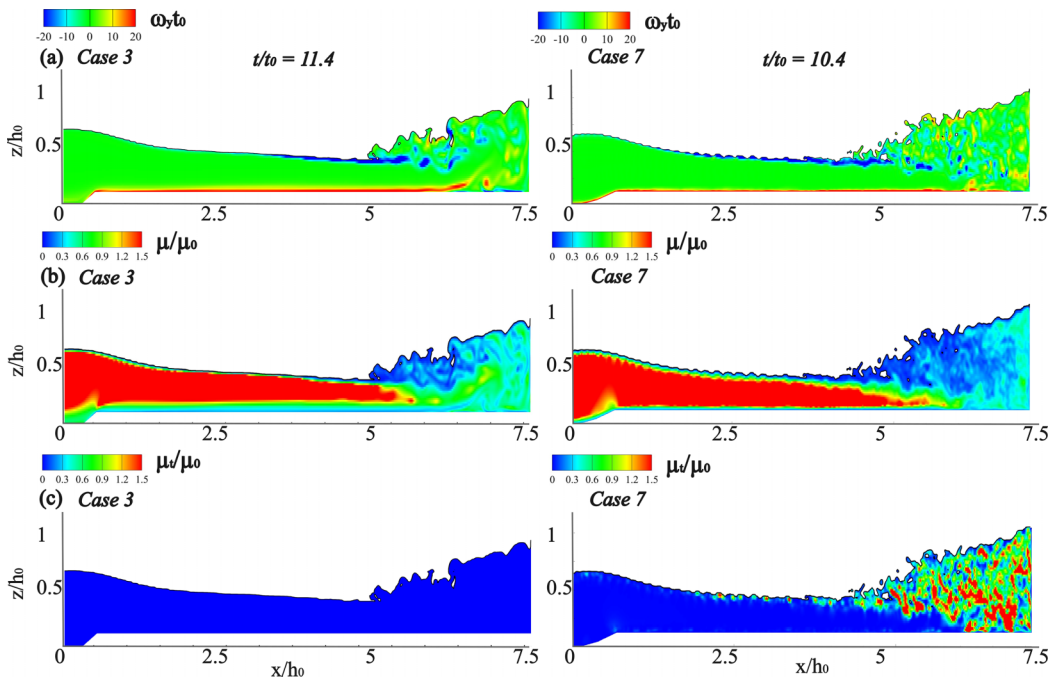


FIG. 16. Scale effects on the structure of the flood wave ($y = \text{const}$ plane) in the case 3 and case 7 simulations. (a) Nondimensional out-of-plane vorticity, $\omega_y t_0$; (b) nondimensional dynamic viscosity; and (c) turbulent viscosity ratio. Results are shown at $t/t_0 = 11.4$ for case 3 ($t/t_0 = 11.4$) and at $t/t_0 = 10.4$ for case 7 when the position of the front of the backward-propagating bore is the same in the two simulations.

(Fig. 18). Once the flow becomes quasilaminar at large distances from the front, turbulence effects are negligible and the bed shear stresses in cases 3 and 7 are very close.

As also observed for gravity-current flows [46], 3D instabilities develop at the front of the dam break wave in all cases as some parts of the front move faster than other parts. This generates fingerlike structures at the front (see Fig. 19), which are similar to the lobe-and-cleft instability observed for gravity currents. A second instability is present in most of the simulations. It consists of the formation of parallel streaks of higher and lower streamwise velocity near the channel bed. The velocity streaks are responsible for the streaky distribution of the bed shear stress observed in Fig. 19 for cases 0, 1, and 7. Such streaks were also observed to form inside turbulent gravity currents [46,48]. The streaks generally extend for some finite distance behind the front. Not surprisingly, such streaks are present in case 0 (see Fig. 19), where the wave contains clear water and the flow is turbulent behind the front. What is notable is that such streaks are also present in all but one of the low-Reynolds-number simulations. For example, 16 streaks can be observed in case 1, slightly smaller than the 20 streaks observed for cases 0 and 7. The increase of the number of streaks with increasing Reynolds number is due to the decrease of the width of the fingerlike eddies forming at the front of the dam break wave. The only simulation where such streaks do not form is case 3. Not surprisingly, this is the most viscous simulation among the low-Reynolds-number simulations conducted with a non-Newtonian fluid. Interestingly, the increase of the Reynolds number does not lead to significant variations of the impact force acting on the endwall (Fig. 20), except for the fact that the wave reaches the endwall earlier in case 7 ($t/t_0 = 4.2$) compared to case 3 ($t/t_0 = 5$).

Most notably, the peak nondimensional impact force is about the same in both simulations. Meanwhile, the energy of the high- and low-frequency oscillations of the impact force is larger in case 7 but this is expected given the wider range of energetic turbulent eddies present near the endwall in the higher-Reynolds-number simulation.

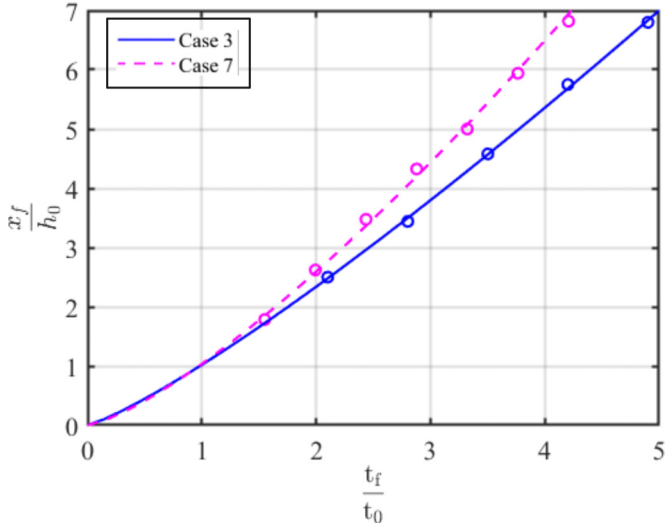


FIG. 17. Scale effects on the temporal variation of the nondimensional front position for the case 3 and case 7 simulations.

V. SUMMARY AND CONCLUSIONS

Fully 3D VOF LESs have been performed to investigate the propagation of non-Newtonian dam break waves generated by the release of mud and their impact with a vertical rigid wall. The viscous flow solver uses the VOF technique to capture the free surface dynamics and the dynamic Smagorinsky model. The mud, a mixture of clay and water, has been described by a shear-thinning power-law model. Most of the numerical simulations were performed at a laboratory scale. An additional test was simulated by increasing the dimensions of the geometrical setup by a factor of 10

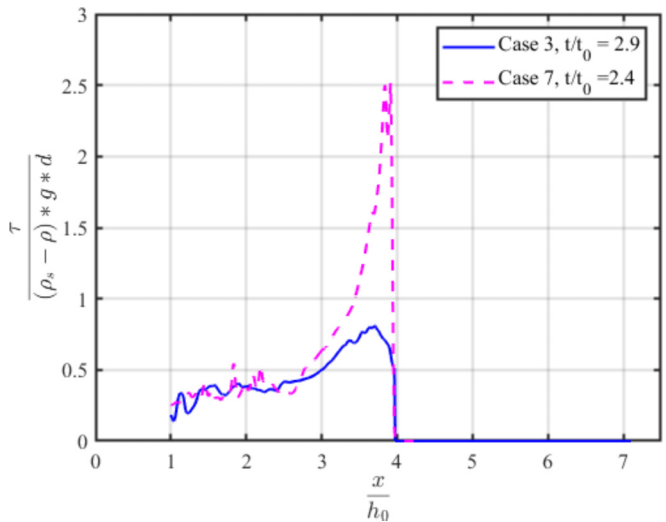


FIG. 18. Scale effects on the nondimensional bed shear stress. The bed shear stresses are compared at different nondimensional times (case 3, $t/t_0 = 2.9$; case 7, $t/t_0 = 2.4$) when wave fronts are situated at the same location ($x/h_0 = 3.8$).

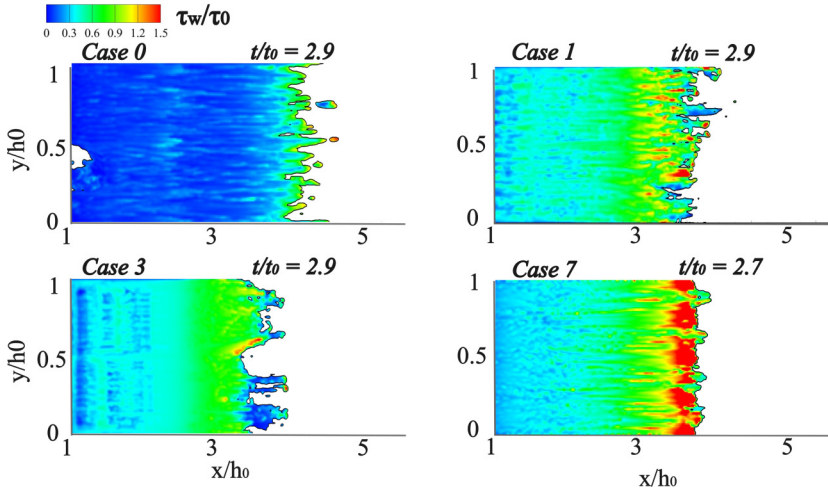


FIG. 19. Bed shear stress distributions ($t/t_0 = 2.9$) for cases 0, 1, 3, and 7. The formation of streamwise streaks behind the front is observed in several cases. Streaks are not observed in case 3, which is the most viscous.

to investigate scale effects. The series of simulations have been designed to analyze in a systematic way the influences of the clay concentration and the initial depth of the non-Newtonian fluid upstream of the lock gate on the wave characteristics. Results also showed important differences between dam break waves of non-Newtonian and Newtonian fluids.

Simulation results conducted with non-Newtonian dam break waves showed that three-dimensional effects are significant near the front, where lobelike structures are present. Moreover, the front position is characterized by a large degree of nonuniformity in the spanwise direction, and velocity streaks are present in the vicinity of the bed in most of the simulations. Independently of the clay concentration and the initial depth of lock fluid, results indicate that the distance traveled by the wave front grows with time following a power law during the propagation phase. However, in the tests conducted with a non-Newtonian fluid, the dimensionless front celerity was smaller

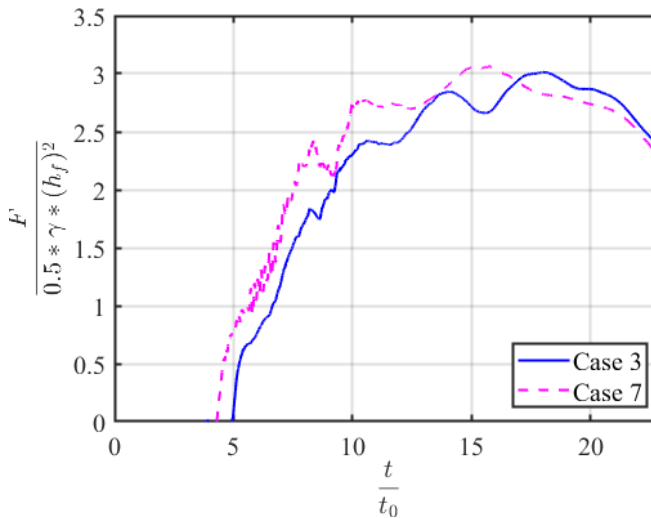


FIG. 20. Scale effects on temporal variation of the nondimensional force acting on the endwall, $F/(0.5\gamma h_f^2)$.

than the one in the clear water case. Moreover, in the presence of clay, the bed shear stress beneath the body of the wave was about two times larger than the corresponding one in clear water. By contrast, the peak values behind the front were found to be comparable. The maximum value of the dimensionless impact force acting on the endwall in the mud simulations was found to be slightly lower than the corresponding one in the clear water case and to decrease with increasing clay concentration. During the propagation phase, the turbulence was found to affect the region close to the front and the bed. Turbulence effects were much stronger during the impact phase, especially in the region situated in between the reflected bore and the endwall, where strong turbulent eddies were generated. A higher nondimensional propagation celerity was observed in the larger-scale, higher-Reynolds-number case compared to the corresponding lower-Reynolds-number case. This was accompanied by higher values of the bed shear stresses in the front region, but comparable values beneath the body of the current. Meanwhile, the maximum value of the nondimensional impact force was not found to be close in the two simulations, which suggests that it can be reliably predicted using laboratory-scale experiments and simulations.

In conclusion, present results indicate that in many field-scale applications where a non-Newtonian (mud) dam break wave forms turbulence effects are significant. Given that RANS models are generally very dissipative and have problems when applied to flows containing regions where the flow is turbulent and laminar, the use of eddy-resolving techniques like LES offers a better alternative for accurately capturing the physics of these flows and predicting quantities of engineering interest. For example, simulations of such flows that do not account for turbulence effects may not be able to accurately predict the amount of sediment entrained by the mud wave. Being able to understand the interaction between a mud wave and an obstacle and to predict variables of engineering interest is also particularly relevant for selecting the most appropriate risk mitigation strategy and for improving the design of protective structures (e.g., rigid and flexible barriers, levees, silt dams, baffles). Since mud flows typically propagate over steep slopes, future work will consider using the present 3D VOF LES model to simulate mud waves propagating in sloped channels. The physics of such flows is more complex due to the possible formation of surface instabilities and strong turbulence generated at the front [52–56], which can also have an important effect on the impact forces induced by mud waves on obstacles placed in their way [57].

-
- [1] C.-O. Ng and C. C. Mei, Roll waves on a shallow layer of mud modelled as a power-law fluid, *J. Fluid Mech.* **263**, 151 (1994).
 - [2] X. Huang and M. H. Garcia, A Herschel–Bulkley model for mud flow down a slope, *J. Fluid Mech.* **374**, 305 (1998).
 - [3] K. F. Liu and C. C. Mei, Slow spreading of a sheet of Bingham fluid on an inclined plane, *J. Fluid Mech.* **207**, 505 (1989).
 - [4] H. Chanson, S. Jarny, and P. Coussot, Dam break wave of thixotropic fluid, *J. Hydraul. Eng.* **132**, 280 (2006).
 - [5] C. Ancey and S. Cochard, The dam-break problem for Herschel–Bulkley viscoplastic fluids down steep flumes, *J. Non-Newtonian Fluid Mech.* **158**, 18 (2009).
 - [6] N. J. Balmforth, R. V. Craster, P. Perona, A. C. Rust, and R. Sassi, Viscoplastic dam breaks and the Bostwick consistometer, *J. Non-Newtonian Fluid Mech.* **142**, 63 (2007).
 - [7] P. Saramito, C. Smutek, and B. Cordonnier, The horizontal dam break problem for slow non-Newtonian power-law fluids, *Int. J. Numer. Anal. Model.* **142**(1-3), 63 (2010).
 - [8] N. Bernabeu, P. Saramito, and C. Smutek, Numerical modeling of non-Newtonian viscoplastic flows: Part II. Viscoplastic fluids and general tridimensional topographies, *Int. J. Numer. Anal. Model.* **11**, 213 (2014).

- [9] M. Greco, C. Di Cristo, M. Iervolino, and A. Vacca, Numerical simulation of mud flows impacting structures, *J. Mountain Sci.* **16**, 364 (2019).
- [10] C. Di Cristo, O. Fecarotta, M. Iervolino, and A. Vacca, Impact dynamics of mud flows against rigid wall, *J. Hydrol.* **612**, 128221 (2022).
- [11] R. B. Minussi and G. de Freitas Maciel, Numerical experimental comparison of dam break flows with non-Newtonian fluids, *J. Braz. Soc. Mech. Sci. Eng.* **34**, 167 (2012).
- [12] C. W. Hirt and B. D. Nichols, Volume of fluid (VOF) method for the dynamics of free boundaries, *J. Comput. Phys.* **39**, 201 (1981).
- [13] N. Schaer, J. Vazquez, M. Dufresne, G. Isenmann, and J. Wertel, On the determination of the yield surface within the flow of yield stress fluids using computational fluid dynamics, *J. Appl. Fluid Mech.* **11**, 971 (2018).
- [14] Y. Liu, N. J. Balmforth, S. Hormozi, and D. R. Hewitt, Two-dimensional viscoplastic dambreaks, *J. Non-Newtonian Fluid Mech.* **238**, 65 (2016).
- [15] R. Valette, A. Pereira, S. Riber, L. Sardo, A. Larcher, and E. Hachem, Viscoplastic dam-breaks, *J. Non-Newtonian Fluid Mech.* **287**, 104447 (2021).
- [16] S. Osher and J.-A. Sethian, Fronts propagating with curvature dependent speed: Algorithms based on Hamilton Jacobi formulations, *J. Comput. Phys.* **79**, 12 (1988).
- [17] S. Shao and E. Y. M. Lo, Incompressible SPH method for simulating Newtonian and non-Newtonian flows with a free surface, *Adv. Water Resour.* **26**, 787 (2003).
- [18] H. A. Barnes, J. F. Hutton, and K. Walters, *An Introduction to Rheology* (Elsevier, Amsterdam, 1989).
- [19] D. Laigle and M. Labbe, SPH based numerical study of the impact of mudflows on obstacles, *Int. J. Erosion Control Eng.* **10**, 56 (2017).
- [20] X. Zhou and Z. Sun, Numerical investigation of non-Newtonian power law flows using B-spline material point method, *J. Non-Newtonian Fluid Mech.* **298**, 104678 (2021).
- [21] J. Tang, P. Lin, and P. Cui, Depth-resolved numerical model of dam break mud flows with Herschel-Bulkley rheology, *J. Mountain Sci.* **19**, 1001 (2022).
- [22] G. E. Blight, Destructive mudflows as a consequence of tailings dyke failures, *Proc. Inst. Civ. Eng. Geotech. Eng.* **125**, 9 (1997).
- [23] M. Rudman, H. M. Blackburn, L. J. W. Graham, and L. Pullum, Turbulent pipe flow of shear-thinning fluids, *J. Non-Newtonian Fluid Mech.* **118**, 33 (2004).
- [24] P. S. Gnanbode, P. Orlandi, M. Ould-Rouiss, and X. Nicolas, Large-eddy simulation of turbulent pipe flow of power-law fluids, *Int. J. Heat Fluid Flow* **54**, 196 (2015).
- [25] T. Ohta and M. Miyashita, DNS and LES with an extended Smagorinsky model for wall turbulence in non-Newtonian viscous fluids, *J. Non-Newtonian Fluid Mech.* **206**, 29 (2014).
- [26] E. Z. Zheng, M. Rudman, J. Singh, and S. B. Kuang, Direct numerical simulation of turbulent non-Newtonian flow using OpenFOAM, *Appl. Math. Modell.* **72**, 50 (2019).
- [27] W. Rodi, G. Constantinescu, and T. Stoesser, *Large-Eddy Simulation in Hydraulics* (CRC Press, Boca Raton, FL, 2013).
- [28] E. Amani, A. Ahmadpour, and M. J. Aghajari, Large-eddy simulation of turbulent non-Newtonian flows: A comparison with state-of-the-art RANS closures, *Int. J. Heat Fluid Flow* **99**, 109076 (2023).
- [29] D. H. Munoz and G. Constantinescu, A fully 3-D numerical model to predict flood wave propagation and assess efficiency of flood protection measures, *Adv. Water Resour.* **122**, 148 (2018).
- [30] D. H. Munoz and G. Constantinescu, 3-D dam break flow simulations in simplified and complex domains, *Adv. Water Resour.* **137**, 103510 (2020).
- [31] T. Lazzarin, G. Constantinescu, L. Di Micco, H. Wu, F. Lavignani, M. Lo Brutto, D. Termini, and D. P. Viero, Influence of bed roughness on flow and turbulence structure around a partially-buried, isolated freshwater mussel, *Water Resour. Res.* **59**, e2022WR034151 (2023).
- [32] H. Wu and G. Constantinescu, Effect of angle of attack on flow past a partially-burrowed, isolated freshwater mussel, *Adv. Water Resour.* **168**, 104302 (2022).
- [33] P. Wu, D. H. Munoz, G. Constantinescu, and Z. Qian, Two-phase flow DES and URANS simulations of pump-intake bay vortices, *J. Hydraul. Res.* **58**, 120 (2020).

- [34] Y. Marschall, G. Constantinescu, R. Boes, and D. F. Vetsch, On the role of free-surface treatment for simulating flow past submerged obstacles, in *Proceedings of the 40th IAHR World Congress* (International Association for Hydro-Environment Engineering and Research, Vienna, 2023), pp. 2282–2289.
- [35] A. Del Gaudio, G. La Forgia, G. Constantinescu, F. De Paola, C. Di Cristo, M. Iervolino, A. Leopardi, and A. Vacca, Modelling the impact of a dam-break wave on a vertical wall, *Earth Surf. Processes Landforms* **49**, 2080 (2024).
- [36] J. Li and J. Xia, Modelling of hyperconcentrated flood routing and channel evolution in the lower Weihe River, *Arabian J. Geosci.* **13**, 1 (2020).
- [37] X. Liu, B. Pan, G. Zhao, P. Zhu, and H. Wang, Hyper-concentration and low-sediment-concentration rivers: Ecosystem stability and driving forces, *Catena* **220**, 106732 (2023).
- [38] J. S. O'Brien and P. Y. Julien, Laboratory analysis of mudflow properties, *J. Hydraul. Eng.* **114**, 877 (1988).
- [39] D. K. Lilly, A proposed modification of the Germano subgrid scale closure method, *Phys. Fluids* **4**, 633 (1992).
- [40] C. Biscarini, S. Di Francesco, and P. Manciola, CFD modelling approach for dam break flow studies, *Hydrol. Earth Syst. Sci.* **14**, 705 (2010).
- [41] H. Ozmen-Cagatay and S. Kocaman, Dam-break flow in the presence of obstacle: Experiment and CFD simulation, *Eng. Appl. Comput. Fluid Mech.* **5**, 541 (2011).
- [42] R. Marsooli and W. Wu, 3-D finite-volume model of dam-break flow over uneven beds based on VOF method, *Adv. Water Resour.* **70**, 104 (2014).
- [43] T. Tokyay, G. Constantinescu, and E. Meiburg, Lock-exchange gravity currents with a high volume of release propagating over a periodic array of obstacles, *J. Fluid Mech.* **672**, 570 (2011).
- [44] S. Muzafferija, Computation of free surface flows using interface-tracking and interface-capturing methods, *Nonlinear Water-Wave Interaction* (WIT Press, Southampton, UK, 1999).
- [45] E. Gonzalez-Juez, E. Meiburg, T. Tokyay, and G. Constantinescu, Gravity current flow past a circular cylinder: Forces, wall shear stresses and implications for scour, *J. Fluid Mech.* **649**, 69 (2010).
- [46] T. Tokyay, G. Constantinescu, and E. Meiburg, Lock-exchange gravity currents with a low volume of release propagating over an array of obstacles, *J. Geophys. Res.: Oceans* **119**, 2752 (2014).
- [47] T. Tokyay and G. Constantinescu, The effects of a submerged non-erodible triangular obstacle on bottom propagating gravity currents, *Phys. Fluids* **27**, 056601 (2015).
- [48] T. Tokyay, G. Constantinescu, and E. Meiburg, Tail structure and bed friction velocity distribution of gravity currents propagating over an array of obstacles, *J. Fluid Mech.* **694**, 252 (2012).
- [49] A. Dai and Y. Huang, On the merging and splitting processes in the lobe-and-cleft structure at a gravity current head, *J. Fluid Mech.* **930**, A6 (2022).
- [50] G. Constantinescu, LES of lock-exchange compositional gravity currents: A brief review of some recent results, *Environ. Fluid Mech.* **14**, 295 (2014).
- [51] J. E. Simpson, Effects of the lower boundary on the head of a gravity current, *J. Fluid Mech.* **53**, 759 (1972).
- [52] M. Iverson, M. Logan, R. G. LaHusen, and M. Berti, The perfect debris flow? Aggregated results from 28 large scale experiments, *J. Geophys. Res.* **115**, 1 (2010).
- [53] C. Di Cristo, M. Iervolino, and A. Vacca, On the applicability of minimum channel length criterion for roll-waves in mud-flows, *J. Hydrol. Hydromech.* **61**, 286 (2013).
- [54] C. Di Cristo, M. Iervolino, and A. Vacca, Gravity-driven flow of a shear thinning power law fluid over a permeable plane, *Appl. Math. Sci.* **33**, 1623 (2013).
- [55] C. Di Cristo, M. Iervolino, and A. Vacca, Instabilities of a dam break wave of power law fluids, *Phys. Fluids* **35**, 103102 (2023).
- [56] K. Steenhauer, T. Tokyay, and G. Constantinescu, Dynamics and structure of planar gravity currents propagating down an inclined surface, *Phys. Fluids* **29**, 036604 (2017).
- [57] B. Yu and V. Chu, Impact force of roll waves against obstacles, *J. Fluid Mech.* **969**, A31 (2023).